

Symmetry-Broken Metamaterial Absorbers as Reflectionless Directional Couplers for Surface Plasmon Polaritons in the Visible Range

Fan Ye,* Michael J. Burns, and Michael J. Naughton*

Gradient-index meta-surfaces have been shown to have the ability to manipulate wavefronts at will in a reflectionless manner in the GHz range, including the extreme example of converting freely propagating waves into surface waves with high efficiency. Upon approaching the optical regime, the gradient-index concept encounters difficulties due to fabrication limitations. Here, it is theoretically and experimentally demonstrated that asymmetric, periodic, two-element metal–insulator–metal structures can serve as reflectionless directional converters between freely propagating visible photons and surface plasmon polaritons (SPPs). Coupling between propagating modes caused by the broken symmetry and localized modes generated by individual elements is shown to be the mechanism of this high-efficiency process, yielding an observed Rabi splitting of ~135 meV. Direct experimental evidence is obtained for reflectionless (<8% measured reflectance) directional SPP coupling in the visible range, with directionality approaching 100%. These results are meaningful for varied applications in integrated nanoplasmonics, plasmonic logic, and plasmonic light harvesting.

1. Introduction

The introduction of the metamaterial (MM) concept has led to an explosion of research over the past decade on the interaction of waves with matter including, for electromagnetic waves, in plasmonics and photonics.^[1–7] Recently, gradient-index meta-surfaces have been shown to have the ability to manipulate wavefronts at will in a reflectionless manner.^[8] As an extreme case of this wavefront tailoring, normally incident waves can be bent 90 degrees onto a sample surface, turning into confined directional surface waves with high efficiency.^[9,10] Due to their gradient nature, each working element must comprise smaller elements with gradually varying geometries.^[8–10] For operation in the visible frequency range, however, fabrication difficulties arise for such designs, as nanoscale structural fidelity is required. As a result, all existing demonstrations have been in the GHz range,^[8–10] for which mm- or cm-scale structures suffice. On the other hand, high-efficiency

directional coupling between propagating photons and surface plasmon polaritons (SPPs) in the visible range is a growing pursuit, due to its perceived essential role in nanoplasmonic and nanophotonic applications.^[11–13]

Here, we demonstrate that asymmetric, two-element, periodic, metal-insulator-metal (MIM) structures, perhaps representing the simplest gradient-index scenario, can serve as reflectionless directional converters between free photons and SPPs operable in the visible frequency range. The simplicity of this two-element MIM structure allows for the fabrication of testable samples for operation with visible light. Simulated dispersion relations of this structure reveal the nature of the high-efficiency coupling process: interactions between propagating modes caused by the broken reflection symmetry (RS) and localized modes generated by individual MIM elements that are

well understood in the language of MM “perfect absorbers”.^[14,15] There are regions in k -space where these interactions are very strong, such that the two modes hybridize to two new quasi-particles,^[16,17] with concomitant Rabi splitting.^[18,19] Experiments on samples with tuned parameters confirm the simulated dispersion maps, and demonstrate a large Rabi splitting. Absolute reflectance measurements under normal incidence with small aperture angle (3.75°) on samples with areas less than $60 \times 60 \mu\text{m}^2$ were carried out using a modified microscope design. This scheme avoids the common problem of averaging over large incident angles when measuring optical properties of small-area samples by conventional methods.^[20] Direct experimental evidence is obtained for reflectionless (less than 8% measured reflectance) directional SPP coupling in the visible range, with more than 88.8% of the channeled SPP energy being directed to the designed direction. Our results are meaningful for integrated nanoplasmonics, plasmonic logic, and plasmonic light harvesting, among others.

2. Results and Discussions

2.1. Localized Mode Analysis

Using the measurement scheme described in Experimental Section, we performed reflectance measurements to study

F. Ye, Dr. M. J. Burns, Prof. M. J. Naughton
Department of Physics
Boston College
140 Commonwealth Avenue
Chestnut Hill, MA 02467, USA
E-mail: fan.ye.bc@gmail.com; naughton@bc.edu



DOI: 10.1002/adom.201400080

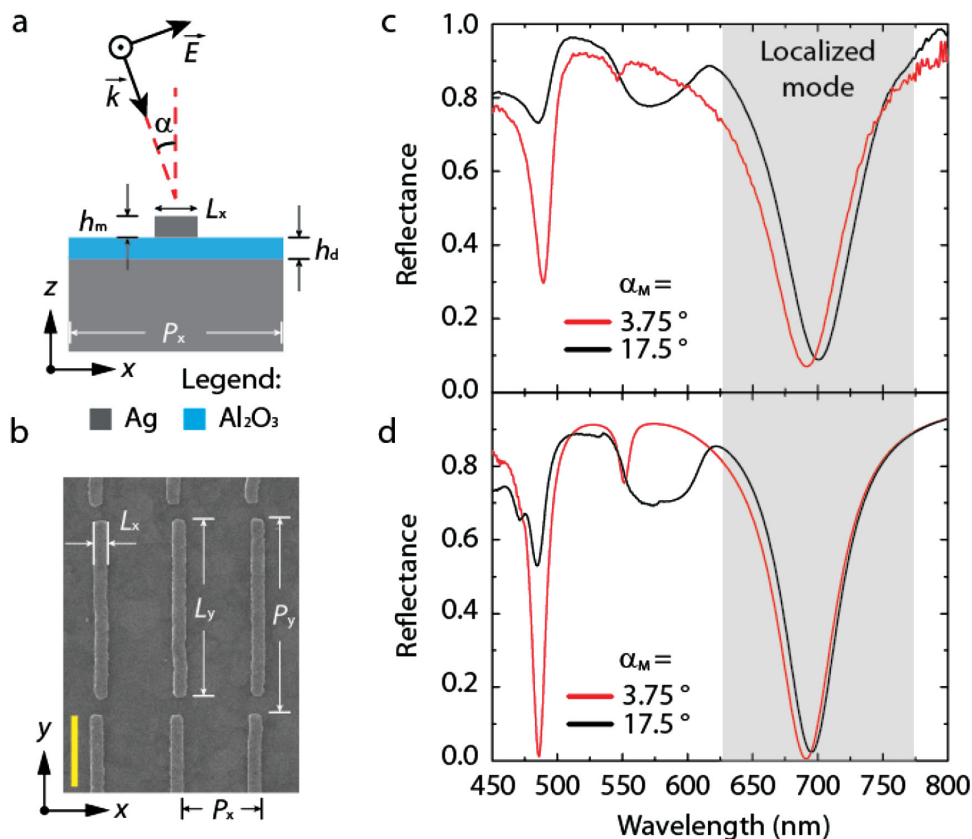


Figure 1. Reflectance measurement of a symmetric single-element MIM array with tuning maximum-incident-angle. a) Schematic of cross-section of one unit cell of a Ag (grey) – Al₂O₃ (blue) – Ag pattern, with transverse magnetic (TM) polarized incident light, indicated by black arrows. b) Top view SEM image of an array of 25-nm-thick Ag bars on 19 nm thick Al₂O₃ and 250 nm thick Ag on a Si substrate. c,d) Measured (c) and simulated (d) reflectance spectra for tuning maximum-incident-angles $\alpha_M = 3.75^\circ$ and 17.5° , under TM polarized incidence. Scale bar in (b), 400 nm. Localized mode is indicated by light grey regions in (c,d).

the localized mode of a single-element symmetric MIM array. **Figure 1a** shows a schematic cross-section of a unit cell of a single-element MIM array, with Ag as the metal and Al₂O₃ the dielectric. A top view scanning electron microscope (SEM) image of a fabricated sample is shown in **Figure 1b**. All relevant parameters are defined in **Figure 1a,b**. **Figure 1c** shows the measured absolute reflectance, while changing the maximum incident angle (i.e., the angle aperture), α_M , of a single-element MIM array with dielectric thickness $h_d = 19$ nm, metal thickness $h_m = 25$ nm, element width $L_x = 68$ nm, element length $L_y = 1000$ nm, horizontal periodicity/pitch $P_x = 450$ nm, and vertical pitch $P_y = 1100$ nm. Absolute reflectance obtained under large α_M (black curve) is distinct from that under small α_M (red curve). Numerical reflectance simulations on a two-dimensional structure with the same cross-section as the real sample, obtained by averaging over individual reflectance spectra with incident angles from 0 to α_M , show good agreement with the measured data (**Figure 1d**). Reflectance minima at wavelength $\lambda \sim 700$ nm are caused by magnetic dipole modes arising from the coupling between the top metal bar and the ground metal plane.^[12] These patch antenna-type SPP modes are localized in the gap between the two metal layers, and are thus less sensitive to variation in incident angle.^[21] The high-efficiency conversion of incident photons to localized SPP gap

modes is well understood in the framework of impedance matching and critical coupling,^[22–24] and has been successfully utilized to make so-called MM “perfect absorbers”.^[14,15] These localized modes (and their interaction with propagating modes) are of main interest in this work, and are thus highlighted by grey shaded regions in **Figure 1c,d**.

Reflectance minima at $\lambda \sim 480$ nm are interacting modes between two neighboring MIM elements, and are thus highly sensitive to the pitch P_x . When increasing the incident angle, the decrease of the effective pitch in the light-propagating direction causes a blueshift of this minimum. Thus, when averaging over larger incident angles, this minimum gets broadened significantly. The minimum above $\lambda \sim 550$ nm emerges only when the incident angle deviates from zero. This feature originates from the coupling of tilted incident waves to propagating surface plasmons. For incident angles closer to the critical angle α_0 , defined in $k_{SPP} = k \sin(\alpha_0) + 2\pi/P_x$, the in-plane k -vector is better matched to that of the propagating SPPs, resulting in improved coupling, and thus a deeper reflectance minimum. Detailed mode analysis is provided in Section I of the Supporting Information (SI). Comparisons between reflectance spectra under normal incidence with various angle apertures provide reliable indications of the localized modes of interest here.

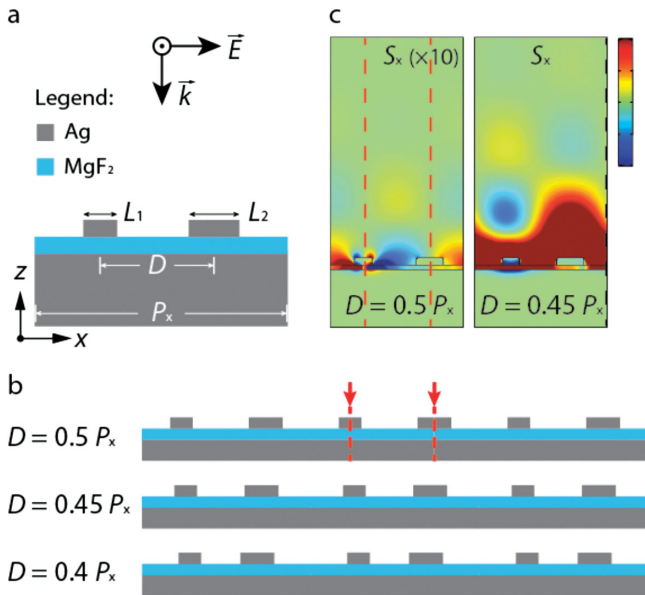


Figure 2. Two-element asymmetric MIM structures. a) Schematic cross-section of a unit cell composed of two elements with different sizes. b) Schematics of three two-element unit cells when tuning D . Note that planes of reflection symmetry exist only when $D = 0.5P_x$, as indicated by red dashed lines. c) Time-averaged power flow density for $D = 0.5P_x$ and $D = 0.45P_x$, under normal incidence. The intensity in the case $D = 0.5P_x$ is amplified by 10. Red dashed lines in (c) indicate planes of reflection symmetry. Color bar in (c), $(-1$ to $1) \times 10^7 \text{ Wm}^{-1}$.

2.2. Broken Symmetry and Propagating Modes

For a periodic system, a unit cell with reflection (mirror) symmetry guarantees the same global RS, like the case shown in Figure 1. Under normal incidence, such a structure generates left- and right-propagating SPPs with the same phase and amplitude with respect to the plane of RS, resulting in complete cancellation. Thus, propagating SPP modes are not expected in structures with RS under normal incidence. To generate propagating SPP modes under normal incidence, one has to break the RS of the system, e.g., by introducing an asymmetric unit cell. Figure 2a shows a simple example of such an asymmetric unit cell, composed of two elements with different sizes. As illustrated in Figure 2b, even for such a structure, RS is still maintained when the separation between two elements is exactly half of the pitch ($D = 0.5P_x$). Two planes of RS are indicated by red dashed lines for the case with $D = 0.5P_x$. Only when D is smaller than $0.5P_x$ is RS broken. Note that by tuning the relation between D and P_x in such a two-element system, one can conveniently tune the system from a state with RS to states without RS. In fact, the deviation of D from $0.5P_x$ can serve as an indicator of the degree of asymmetry of the system. Figure 2c shows profiles of the x component of the time-averaged power flow density S_x for $D = 0.5P_x$ and $D = 0.45P_x$ under the same incident condition and with all other parameters unchanged ($h_d = 20 \text{ nm}$, $h_m = 30 \text{ nm}$, $L_1 = 75 \text{ nm}$, $L_2 = 115 \text{ nm}$ and $P_x = 566 \text{ nm}$). For the symmetric case ($D = 0.5P_x$), S_x changes signs with respect to the symmetry planes, indicating cancellation of left- and right-going SPPs. As a result, only localized SPPs are formed in such a system. For the asymmetric case ($D = 0.45P_x$),

S_x forms a continuous band along the metal surface, revealing constructive interference of the generated SPPs that leads to directional propagation. The red color of the power flow density profile indicates that the generated SPPs are propagating in the positive x direction.

2.3. Interactions between Propagating and Localized Modes

To deepen our understanding of this phenomenon, we generated simulations of reflectance spectrum color maps for two-element MIM cells with $L_1 = 75 \text{ nm}$, $L_2 = 115 \text{ nm}$, while tuning the periodicity P_x (and thus the in-plane reciprocal momentum vector $k_{11} = 2\pi/P_x$). This reveals the dispersion relations of the propagating and localized modes as shown in Figure 3. From Figure 3a we see that, for the symmetric case $D = 0.5P_x$, only localized SPP modes are present, with the upper branch of reflectance minima corresponding to local resonances at the shorter sub-element (L_1), and the lower branch to resonances at the longer sub-element (L_2). Once RS is broken by deviating from $D/P_x = 0.5$, an additional branch emerges in the reflectance color map, representing a new propagating mode (as shown in Figure 3b and c). The broken RS in the two-element structure has thus created a new mode that supports propagating SPPs, which were forbidden by symmetry in the symmetric system. One important feature of this propagating-mode branch is its intersection with the localized branches. Such intersections on an ω - k dispersion diagram indicate the locations of enhanced interactions, due to the simultaneous satisfaction of the laws of conservation of momentum and energy at those points. As the asymmetry of the structure is increased (by decreasing D/P_x further from 0.5), the interaction between the propagating mode and the localized mode of the shorter element begins to hybridize these modes into two new quasi-particles,^[16,17] as clearly shown in Figure 3c.

A strong interaction promises a high energy transfer rate between the two interacting modes. We would thus expect photon-SPP conversion to be most efficient at the intersections of the propagating and localized modes. To evaluate the strength of the generated SPP, we define a quantity I_1 , obtained by integrating the x -component of the time-averaged power flow density over the right-hand-side boundary of a unit cell (indicated by the black dashed line in Figure 2c, $D = 0.45P_x$ case). Figure 3d–f shows color maps of I_1 in accordance with the cases in Figure 3a–c. It is not surprising to see a featureless blank map for $D = 0.5P_x$ (the symmetric case) in Figure 3d, where no propagating SPPs are generated and I_1 is zero everywhere. When RS is broken, branches of non-zero I_1 emerge (Figure 3e,f), with extreme values (maxima and minima) taking place at the intersections of the propagating and localized modes, as expected. At the intersection of the propagating mode with the localized mode of the shorter element L_1 (longer element L_2), the generated SPPs travel in the $+x$ ($-x$) direction, resulting in the red (blue) streaks in Figure 3e,f. Thus, a properly designed two-element asymmetric MIM structure, when working at an interaction zone, becomes a high-efficiency, reflectionless, photon-SPP coupler. A detailed discussion of the optimum separation D for directional SPP coupling is provided in the SI, section III.

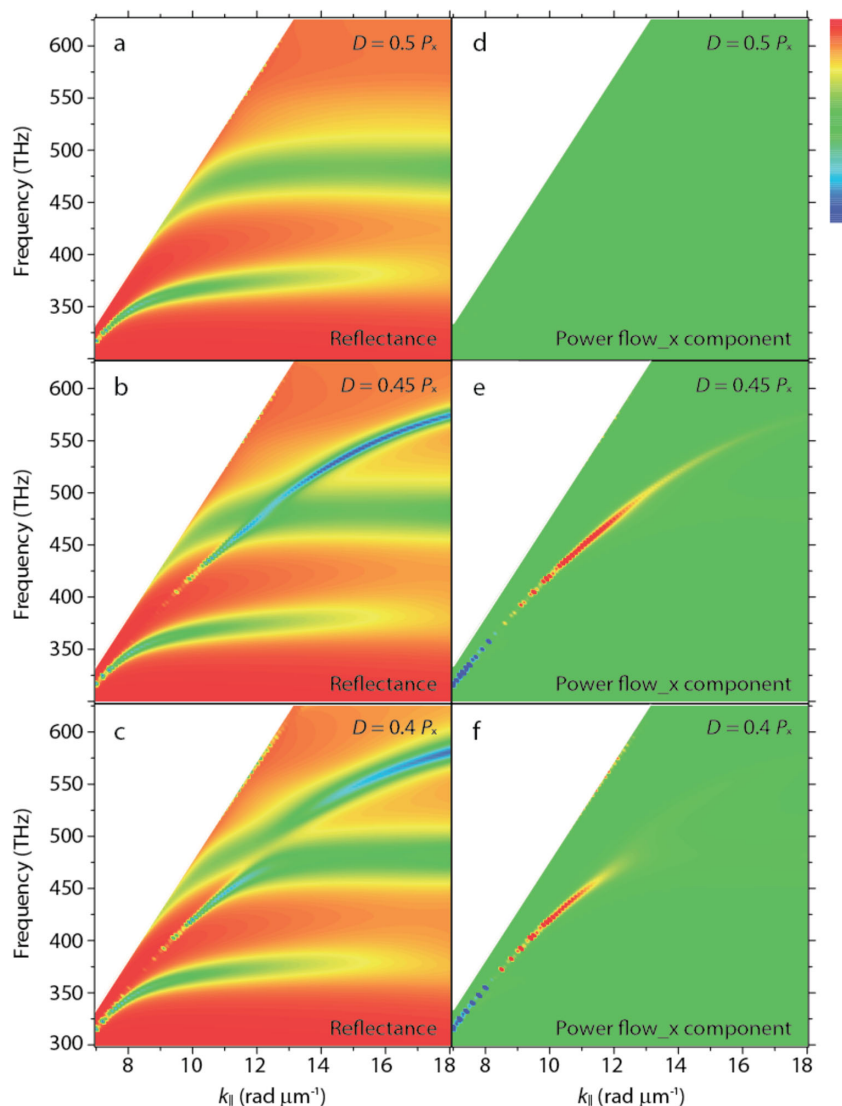


Figure 3. Simulated dispersion bands for asymmetric structures with tuned asymmetry. a–c) Simulated reflectance color maps for two-element asymmetric two-element cells with $L_1 = 75$ nm, $L_2 = 115$ nm, $h_d = 20$ nm, $h_m = 30$ nm, P_x tuned from 350 to 900 nm, with $D = 0.5P_x$ in (a), $0.45P_x$ in (b), and $0.4P_x$ in (c). The in plane momentum vector k_{11} is obtained from: $k_{11} = 2\pi/P_x$. d–f) Simulated color maps of x-component of time-averaged power flow density integrated over the boundary of a unit cell, for structures corresponding to (a)–(c). Unconfined modes above the linear ω - k light line are blocked by white triangles to focus on the confined modes below the light line for all panels. Color bars from blue to red: in (a–c), 0 to 1; in (d–f), (–2 to 2) W, with regions greater (less than) or equal to 2 (–2) W shown as red (blue).

Guided by the simulation results, we fabricated arrays of two-element Ag-MgF₂-Ag MIM patterns with $h_d = 20$ nm, $h_m = 30$ nm, $L_1 = 60$ nm, $L_2 = 100$ nm, $L_y = 1000$ nm, $D = 0.45P_x$, $P_y = 1100$ nm, and P_x tuned from 400 to 880 nm, with a 20 nm step size (as shown in Figure 4a). In fabricating this structure, we chose to use thermally evaporated MgF₂ as the dielectric layer, due to its low loss in the visible range,^[25] which is favorable for a propagating SPP mode. We measured their absolute reflectance spectra via our modified scheme (Experimental Section), and plotted them in Figure 4b. Two branches of localized modes and one branch of a propagating mode are clearly seen in Figure 4b, with the intersection regions showing

the lowest reflectance (blue). Figure 4c and d show another tuning sample with $L_1 = 75$ nm, $L_2 = 115$ nm and all other parameters unchanged. The enlarged L_1 and L_2 values redshift the two localized branches, pushing the lower branch caused by L_2 out of the shown frequency range. The propagating mode is still clearly present, along with the intersection region. Note that all the localized modes are redshifted (i.e., occurring at lower frequencies) when k_{11} increases, as opposed to the simulations, where localized modes approach flat lines for large enough k_{11} . This effect is caused by the artifact of the electron beam lithography process employed in the fabrication: when two elements are closer to each other, their actual individual sizes under the same resist exposure conditions become larger due to local charging effects.^[26] Thus, as k_{11} increases, the actual sizes for L_1 and L_2 increase, redshifting the branches. The good agreement between measured and simulated reflectance spectrum color maps validates our physical picture of the high-efficiency photon-SPP conversion process.

To quantify the interaction strength between the propagating and localized modes, and to calculate the coupling efficiency from free photons to propagating SPPs, we fitted the measured data based on temporal coupled mode theory,^[23,27] and extracted the Rabi splitting.^[18] Figure 5a shows the upper (squares) and lower (circles) branches of reflectance minima fitted by two Lorentz line shapes (Experimental Section):

$$R_i = R_B \frac{(\gamma_{ei} - \gamma_{oi})^2 + (\omega - \omega_{oi})^2}{(\gamma_{ei} + \gamma_{oi})^2 + (\omega - \omega_{oi})^2}, \quad (1)$$

with γ_e and γ_o being the external and intrinsic decay rates of the structure, respectively, ω_0 the resonance frequency of the structure, and R_B ($O(1)$) introduced as a fitting parameter to compensate for uncaptured mechanisms leading to background reflectance. The subscript $i = 1, 2$ labels the propagating and localized modes, respectively. A large Rabi splitting of ~ 135 meV is obtained from the fitted data (i.e., amounting to $\sim 10\%$ of the incident photon energy).^[18] The crossing between linewidths of the upper and lower modes shown in Figure 5b is a strong indication of the Rabi splitting.^[18] A fitting example with $P_x = 540$ nm is shown in Figure 5c, with the black dashed line indicating the propagating mode, and the red solid line representing the localized mode. The coupling efficiency is calculated (Experimental Section) and plotted by the green dashed-dotted line in Figure 5c, reaching a maximum of 76%.

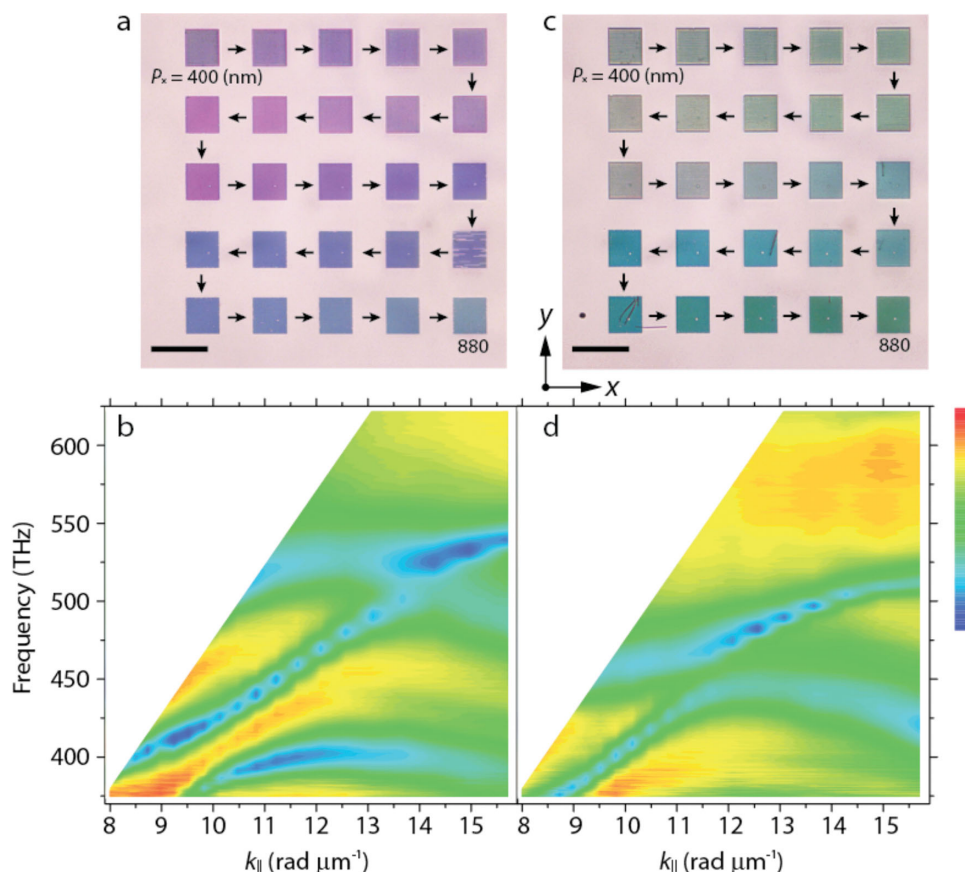


Figure 4. Measured reflectance color map demonstrating the propagating and localized SPP modes. a,b) Bright field optical image under x-polarized incidence (a) and measured reflectance color map under x-polarized incidence (b) of arrays of two-element Ag-MgF₂-Ag patterns with $L_1 = 60$, $L_2 = 100$ nm, $D = 0.45P_x$, P_x tuned from 400 to 880 nm, with a 20 nm step size. c,d) Bright field optical image (c) and measured reflectance color map (d) under x-polarized incidence of two-element Ag-MgF₂-Ag patterns with $L_1 = 75$, $L_2 = 115$ nm, $D = 0.45P_x$, P_x tuned from 400 to 880 nm, with a 20 nm step size. Black arrows in (a) and (c) indicate the direction of increasing P_x . Each array area in (a) and (c) is $60 \times 66 \mu\text{m}^2$. Scale bars in (a) and (c), 100 μm ; Color bars in (b) and (d), absolute reflectance from 0 (blue) to 1 (red).

2.4. Experimental Verification of Reflectionless Directional SPP Generation

Time reversal symmetry of electromagnetic waves tells us that a structure that reflectionlessly couples $-z$ propagating photons to $+x$ propagating SPPs can also serve as a perfect coupler for $-x$ propagating SPPs to $+z$ propagating photons. On this basis, we proposed a simple structure made of arrays of the two-element asymmetric MIM unit cells shown in Figure 4c to experimentally demonstrate reflectionless directional generation of SPPs. As shown in Figure 6a,b, our structure consists of three sets of 44 μm -long Ag bars, with the center set composed of 6 unit cells in the x direction, and the outer two sets 10 unit cells each. Note that the directionality of the MIM unit cells in the center set is pointing to the right with the outer two sets pointing towards the center, so that the center set, when illuminated, serves as the photon-SPP coupler, and the outer two as SPP-photon couplers. As shown in Figure 6c, when x-polarized $\lambda = 642$ nm photons are coupled to the center set, they convert to right-going SPPs with high efficiency, resulting in a dark region (low reflectance) in the otherwise bright center of

the illuminated zone. Reflectance of the center set can be read directly from Figure 4d. With $P_x = 550$ nm and $\lambda = 642$ nm corresponding to $k_{11} = 11.4 \text{ rad } \mu\text{m}^{-1}$ and frequency = 467 THz, the obtained reflectance is 8%, locating at the interaction zone between the propagating mode and the localized mode caused by the smaller element (L_1). When the right-going SPPs arrive at the reversely arranged MIM unit cells on the set to the right, they are scattered into freely propagating photons that travel into the far field, resulting in the bright streak in the right-hand-side set. In strong contrast, the left-hand-side set is nearly completely dark, suggesting no SPPs are directed to the left that could transform/scatter as photons. The ratio of light intensities integrated over the right- and the left-hand-side sets reveals that 88.8% of the SPPs generated by the center set were directed to the right, and only 11.2% to the left. In another sample, these values were 99.7% to the right and 0.3% to the left. As discussed in Figure 3, if we increase the incident wavelength, we will see the center set start to direct SPPs to both directions; and if we further increase the incidence wavelength, we will see the center set directs SPPs to the left hand side (as discussed in detail in SI, Section IV).

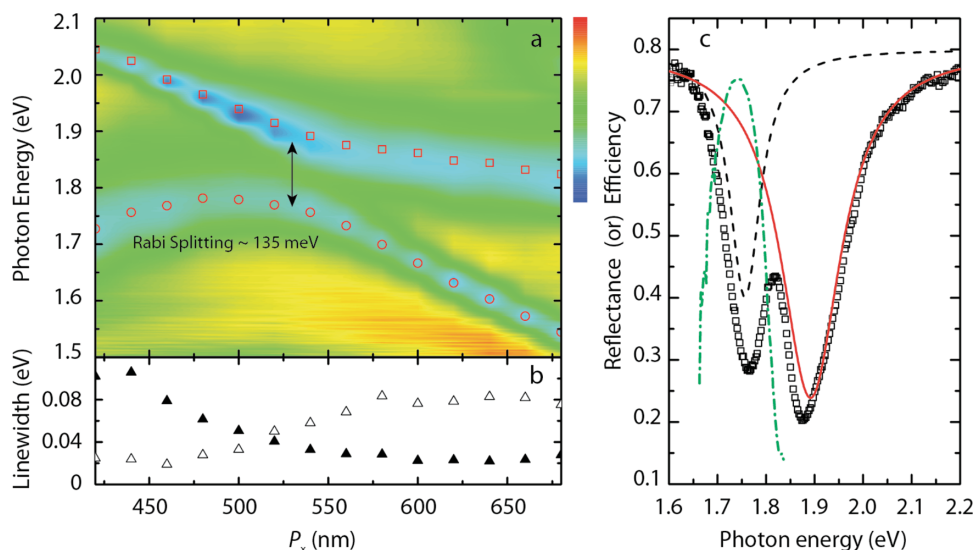


Figure 5. Rabi splitting and coupling efficiency. a) Measured reflectance color map of arrays of two-element Ag-MgF₂-Ag patterns with parameters defined for Figure 4d. Squares (circles) indicate fitted upper (lower) branch of reflectance minima, showing a Rabi splitting of ~135 meV. b) Linewidths of the upper (open triangles) and lower (solid triangles) branches extracted from fittings in (a). c) Measured and fitted reflectance of data shown in (a), at $P_x = 540$ nm. Open black squares indicate measured reflectance, dashed black (solid red) line indicates fitted reflectance for the lower (upper) mode, and green-dashed-dotted line indicates the calculated coupling efficiency into the propagating mode. Color bar in (a) indicates reflectance from 0 (blue) to 1 (red).

2.5. Quality Factor and Decay Length

Another important feature of the propagating SPP mode is its high quality factor Q as compared to the localized modes. This is because the mode cavity for a localized mode is restricted by the size of the resonating element, while for a propagating mode, the cavity size is greatly enlarged, allowing for much more energy to be stored in each resonant cycle. From the measured results in Figure 5, we can extract the Q values for both localized and propagating modes: $Q = \omega_0/\gamma_0$. For $P_x = 460$ nm, we obtain $Q = 105.6$ for the propagating mode at 1.99 eV, and $Q = 22.4$ for the localized mode at 1.77 eV. When properly designed, asymmetric MIM structures can thus be utilized as high- Q MM “perfect absorbers” in the visible regime.^[28]

The reflectionless conversion of a free photon to an SPP is a conversion from a 2D wavefront to a 1D one, which in itself has merit in terms of energy concentration. Combined with various existing techniques for surface plasmon focusing,^[29,30] the 1D wavefront of the SPP can be further confined to a point (0D), to realize the concentration of photon energy from a macroscopic area to a (sub-)microscopic point. This scheme is different from the conventional single-element nanoparticle plasmonic resonator, where energy is concentrated into a nanoscale resonator from only within an area within a few wavelengths of the incident light.^[31] The fact that the power flow (x component) integrated over the unit cell boundary is larger than the total power (1 W) input to the cell (as shown in Figure 3d–f) seems counter-intuitive at first. However, we argue here that this is, in fact, a physical result caused by the conversion of a 2D input wavefront to a directional 1D wavefront by the asymmetric MIM structure.

The excess x -directional power flow comes from the propagating SPPs generated in the adjacent unit cells. Denoting the power flow density along the input port as S_y , the total power absorbed by each unit cell is: $I_0 = (1 - R_t)P_x S_y$, with $P_x S_y$ set to be 1 W. If we assume the decay length of the directional SPP to be ℓ , then the power flow integrated over a unit cell boundary is:

$$I_1 = (1 - R_t) \int_{-\infty}^0 e^{x/\ell} \eta S_y dx = (1 - R_t) \ell \eta S_y, \quad (2)$$

(setting the position of the boundary as $x = 0$). We can thus calculate the decay length of the directional SPP mode via $\ell = P_x I_1 / (\eta I_0)$, a quantity that reaches 4.4 μm for structure with $P_x = 582$ nm (calculated in SI, Section V). Thus, this asymmetric MIM structure is able to collect the input photon energy over a 4.4 μm range and concentrate it into a line along the sample surface.

3. Conclusion

We have studied the role of reflection symmetry in surface plasmon polariton generation. We have demonstrated a high-efficiency coupling channel between free photons and directional propagating surface plasmons that are confined to a metal/insulator interface. We have realized reflectionless photon-SPP conversion in the visible range based on a two-element asymmetric MIM structure. Our results may bring new possibilities to subjects such as high- Q MM “perfect absorbers”, plasmonic energy harvesting, and plasmonic logic, among others.

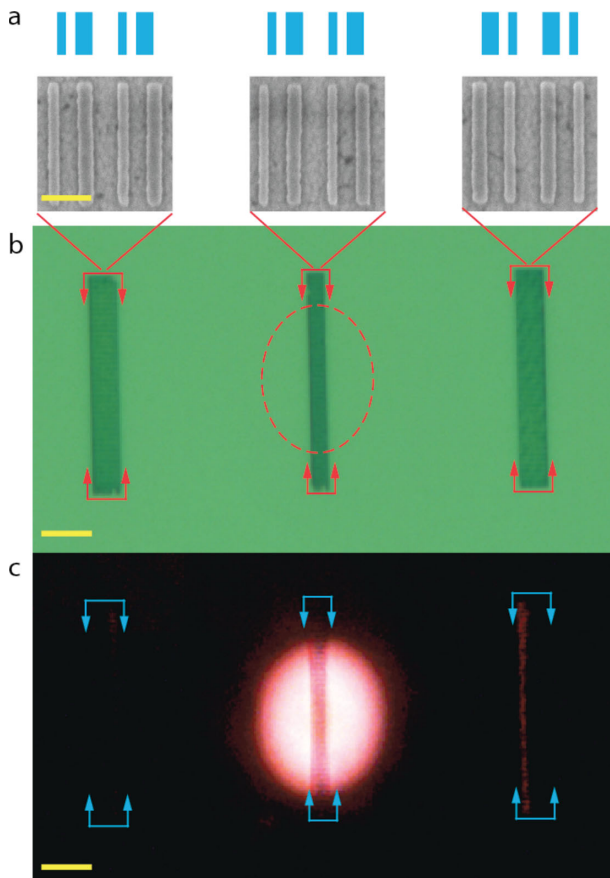


Figure 6. Experimental demonstration of reflectionless directional SPP coupling. a) Top view SEM images of two-element asymmetric Ag-MgF₂-Ag patterns corresponding to regions indicated in (b). Geometric parameters for each unit cell are $L_1 = 75$ nm, $L_2 = 115$ nm, $L_y = 1000$ nm, $P_x = 550$ nm, $P_y = 1100$ nm, $h_d = 20$ nm, and $h_m = 30$ nm. The blue bars on top are schematics indicating the directionality of the corresponding unit cells. b) Bright field optical image of three sets of 44 μm -long bars comprising the two-element directional SPP couplers, with the center set designed to direct energy to the right, and the outer two sets toward the center. The center set consists of 6 unit cells, and the outer sets 10 unit cells each. c) Optical image of the same area as (b), with confined $\lambda = 642$ nm light illuminating the center area as indicated by a red dashed line in (b). Re-scattered light is clearly seen in the right-hand-side set while, in strong contrast, no light is seen in the set on the left. Blue & red arrows are guides to the eye indicating the outer contours of the three sets in (b) and (c). Scale bars in (a), 400 nm; in (b) and (c), 10 μm .

4. Experimental Section

Sample Fabrication: Polished silicon wafers were coated with 250 nm thick Ag using electron beam evaporation. Dielectric coating immediately followed, with 19 nm thick Al₂O₃ coated by atomic layer deposition (ALD), or 20 nm MgF₂ by thermal evaporation. We spun PMMA 495 A3 resist on the substrate at 4500 rpm and baked it at 180 °C for 90 s. Electron beam lithography was used to define the metal patterns, and 25 (30) nm Ag layers were deposited on patterned PMMA-Al₂O₃-Ag (MgF₂-Ag) substrates using electron beam evaporation. A lift-off process was performed using acetone on a 75 °C hot plate for about 20 min. Acetone was stirred gently with a glass pipette during the lift-off process.

Optical Measurement: The characterization of absolute reflectance of a sample with micrometer-sized area under normal incidence is non-trivial. In the IR, UV and X-ray ranges, Schwarzschild-type reflective lenses

are widely adopted for small-size samples, setting a lower limit to the incident angle, usually between 10° and 30°. [32,33] In the visible regime, objectives with high magnification are commonly used to match the field of view (FOV) to the small areas of the samples under investigation. However, a high-magnification lens comes with a high numerical aperture (NA), leading to a large upper limit for the incident angle. [34] Thus, for a small incident angle measurement, a low-magnification lens is overwhelmingly large compared to a micrometer-scale sample area. As shown in Figure 7a, we showed that, instead of shrinking the FOV, one can restrict the size of the illuminated area to match the sample size. This required a critical illumination scheme, where a light source forms a real image on the sample plane. [35] Optical measurements were performed under a modified Leica DM6000M microscope, as shown in Figure 7a. For reflectance measurements, broadband light from a halogen lamp was coupled into the system through an optical fiber with NA = 0.2 to ensure uniformity of illumination spot, then restricted by a 556 μm -diameter pinhole. An Ocean Optics Maya2000 Pro spectrometer was used to collect the spectrum data. Reflected light was collected using a 10 \times Zeiss microscope objective with NA = 0.30, corresponding to a maximum incidence angle of $\alpha_0 = 17.5^\circ$. As shown in Figure 7b,c, the spot size of the light source is $R_0 = 133.3$ μm without the pinhole, and $R_p = 27.8$ μm with the pinhole. From the geometric relation $\tan\alpha_0/\tan\alpha_1 = R_0/R_p$, we obtained the restricted maximum incident angle: $\alpha_1 = 3.75^\circ$. For calibration of absolute reflectance, we first measured the reflection signal of the sample, then normalized it to the reflection signal from a Ag mirror (ThorLabs PF10-03-P01). The obtained reflectance was then calibrated using the reflectance spectrum of the Ag mirror, thus yielding an absolute, rather than arbitrary, reflectance measurement. The single color light source used for the data in Figure 6 was obtained by sending broadband light from the halogen lamp through an Optometrics TLS 25C tunable light source with an output bandwidth of 3 nm.

Numerical Simulations: Full-field electromagnetic simulations were performed using COMSOL Multiphysics (RF Module), simulation software based on the finite element method (FEM). A unit cell of the investigated structure was simulated using periodic boundary conditions along the x axis, and perfectly matched layers along the propagation of electromagnetic waves (z axis). A plane wave port was used to launch plane waves toward the unit cell along the -z direction, and reflectance was calculated from the S-parameters obtained from the incident port. The edge blunting effect was taken into consideration by rounding the top corners of metal elements with 8 nm radius. The localized and propagating modes studied in this paper were not sensitive to the bluntness of these corners, as detailed in SI, Section VI, assuring a more stable result against nanofabrication imperfections. All simulations reported in the main text are performed in 2D layouts, with the input port inputting total power of 1 W. Note that for a 2D simulation, the power flow density has units of Wm^{-1} . [27] In all of the simulations, we employed a triangular mesh with a minimum mesh size of 1 nm. Interpolations of experimentally-obtained optical constants were assigned for all the materials used in simulations, with Ag taken from Ref. [36], Al₂O₃ from Ref. [37], and MgF₂ from Ref. [25]. The loss tangent of the ALD-coated Al₂O₃ was taken to be 0.04, according to Liu et al. [15] The relative permittivity and permeability of air were taken to be 1.

Temporal Coupled Mode Theory: The scattering process of a resonance to a continuum input can be described by the temporal coupled mode theory: [23]

$$\frac{da}{dt} = (i\omega_0 - \gamma_0 - \gamma_e)a + \sqrt{2\gamma_e}s_+, \quad (3)$$

$$s_- = -s_+ + \sqrt{2\gamma_e}a, \quad (4)$$

where a is the local resonance amplitude, ω_0 the resonance frequency, γ_0 the decay rate due to local loss, γ_e the decay rate due to escaping power, s_+ the input power amplitude, and s_- the reflected power amplitude. From the above equation, we can solve for reflectance amplitude:

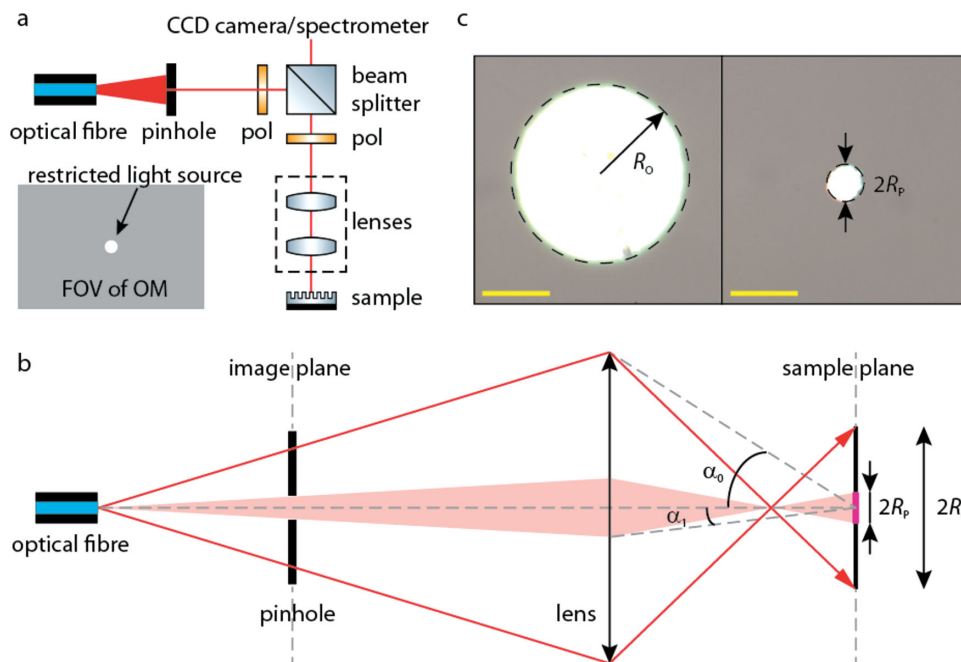


Figure 7. A modified reflectance measurement scheme for small samples with small-angle incidence. a) Layout of measuring scheme used to obtain the reflectance of a sample with small area. The illumination from a halogen broadband light source or a tunable light source is coupled into the system through an optical fiber, and then restricted by a pinhole on the image plane, which is confocal with the CCD camera and spectrometer. The restricted illuminated area is schematically shown in the lower left inset of (a) (white circle), in contrast to the much larger field of view (FOV) of an optical microscope (OM) (grey box). b) Simplified optical path for the modified optical microscope to illustrate the role of the pinhole in restricting both illumination spot size and maximum incident angle. c) Optical images of illuminated spot (white spot) from the optical fiber on a Ag mirror with dimmed background illumination, for situations with (right) and without (left) the pinhole. Scale bars in (c), 100 μm .

$$r = \frac{s_-}{s_+} = \frac{(\gamma_e - \gamma_0) - i(\omega - \omega_0)}{(\gamma_e + \gamma_0) - i(\omega - \omega_0)}, \quad (5)$$

and thus,

$$R = |r|^2 = \frac{(\gamma_e - \gamma_0)^2 + (\omega - \omega_0)^2}{(\gamma_e + \gamma_0)^2 + (\omega - \omega_0)^2}. \quad (6)$$

When the external and intrinsic loss rates match, the local resonance reaches “critical coupling” with the input continuum, resulting in zero reflectance.^[24] In the fitting shown in Figure 5, we have introduced a fitting factor $R_B < 1$ to account for unknown factors in realistic fabricated sample and measurement. Denoting the total reflectance of the structure as R_t , and the reflectance of the localized (propagating) mode as R_2 (R_1), we then have $R_t = R_1 + R_2 - R_B$, and the coupling efficiency of the input energy into the propagating mode can be calculated by:

$$\eta = \frac{(R_B - R_t) - (R_B - R_2)}{R_B - R_t}. \quad (7)$$

Supporting Information

Supporting Information is available from the Wiley Online Library or from the author.

Acknowledgements

The authors acknowledge partial support from W. M. Keck Foundation, and thank Prof. K. Kempa and Dr. J. M. Merlo at Boston College for discussions.

Received: February 17, 2014

Revised: June 26, 2014

Published online: July 29, 2014

- [1] J. B. Pendry, A. J. Holden, D. J. Robbins, W. J. Stewart, *IEEE Trans. Microwave Theory Tech.* **1999**, *47*, 2075.
- [2] D. R. Smith, W. J. Padilla, D. C. Vier, S. C. Nemat-Nasser, S. Schultz, *Phys. Rev. Lett.* **2000**, *84*, 4184.
- [3] J. B. Pendry, *Phys. Rev. Lett.* **2000**, *85*, 3966.
- [4] J. Li, C. T. Chan, *Phys. Rev. E* **2004**, *70*, 055602.
- [5] J. B. Pendry, D. Schurig, D. R. Smith, *Science* **2006**, *312*, 1780.
- [6] S. Zhang, D. A. Genov, C. Sun, X. Zhang, *Phys. Rev. Lett.* **2008**, *100*, 123002.
- [7] J. Baudon, M. Hamamda, J. Grucker, M. Boustimi, F. Perales, G. Dutier, M. Ducloy, *Phys. Rev. Lett.* **2009**, *102*, 140403.
- [8] C. Pfeifer, A. Grbic, *Phys. Rev. Lett.* **2013**, *110*, 197401.
- [9] S. Sun, Q. He, S. Xiao, Q. Xu, X. Li, L. Zhou, *Nature Mat.* **2012**, *11*, 426.
- [10] J. Wang, S. Qu, H. Ma, Z. Xu, A. Zhang, H. Zhou, H. Chen, Y. Li, *Appl. Phys. Lett.* **2012**, *101*, 201104.
- [11] F. Lopez-Tejiera, S. G. Rodrigo, L. Martin-Moreno, F. J. Garcia-Vidal, E. Devaux, T. W. Ebbesen, J. R. Krenn, I. P. Radko, S. I. Bozhevolnyi, M. U. Gonzalez, J. C. Weeber, A. Dereux, *Nature Phys.* **2007**, *3*, 324.
- [12] Y. Liu, S. Palomba, Y. Park, T. Zentgraf, X. Yin, X. Zhang, *Nano Lett.* **2012**, *12*, 4853.
- [13] J. Lin, J. P. Balthasar Mueller, Q. Wang, G. Yuan, N. Antoniou, X.-C. Yuan, F. Capasso, *Science* **2013**, *340*, 331.
- [14] N. I. Landy, S. Sajuyigbe, J. J. Mock, D. R. Smith, W. J. Padilla, *Phys. Rev. Lett.* **2008**, *100*, 207402.
- [15] X. Liu, T. Starr, A. F. Starr, W. J. Padilla, *Phys. Rev. Lett.* **2010**, *104*, 207403.

- [16] E. Prodan, C. Radloff, N. J. Halas, P. Nordlander, *Science* **2003**, *302*, 419.
- [17] W. Zhou, J. Y. Suh, Y. Hua, T. W. Odom, *J. Phys. Chem. C* **2013**, *117*, 2541.
- [18] A. Christ, S. G. Tikhodeev, N. A. Gippius, J. Kuhl, H. Giessen, *Phys. Rev. Lett.* **2003**, *91*, 183901.
- [19] A. Christ, T. Zentgraf, S. G. Tikhoddev, N. A. Gippius, J. Kuhl, H. Giessen, *Phys. Rev. B* **2006**, *74*, 155435.
- [20] K. Aydin, V. E. Ferry, R. M. Briggs, H. A. Atwater, *Nat. Commun.* **2011**, *2*, 517.
- [21] J. Britt Lassiter, F. McGuire, J. J. Mock, C. Ciraci, R. T. Hill, B. J. Wiley, A. Chilkoti, D. R. Smith, *Nano Lett.* **2013**, *13*, 5866.
- [22] M. J. Lockyear, A. P. Hibbins, J. R. Sambles, *Phys. Rev. Lett.* **2009**, *102*, 073901.
- [23] H. A. Haus, *Waves and Fields in Optoelectronics*, Prentice Hall Inc., New Jersey, USA **1984**, Ch. 7.
- [24] C. Wu, B. Neuner III, G. Shvets, J. John, A. Milder, B. Zollars, S. Savoy, *Phys. Rev. B* **2011**, *84*, 075102.
- [25] J. M. Siqueiros, R. Machorro, L. E. Regalado, *Appl. Opt.* **1988**, *27*, 2549.
- [26] K. D. Cummings, M. Keirsh, *J. Vac. Sci. Technol. B* **1989**, *7*, 1536.
- [27] Z. Ruan, S. Fan, *Phys. Rev. Lett.* **2010**, *105*, 013901.
- [28] A. Moreau, C. Cristian, J. J. Mock, R. T. Hill, Q. Wang, B. J. Wiley, A. Chilkoti, D. R. Smith, *Nature* **2012**, *492*, 86.
- [29] T. Zentgraf, Y. Liu, M. H. Mikkelsen, J. Valentine, X. Zhang, *Nature Nanotech.* **2011**, *6*, 151.
- [30] Z. Fang, Q. Peng, W. Song, F. Hao, J. Wang, P. Nordlander, X. Zhu, *Nano Lett.* **2011**, *11*, 893.
- [31] K. Li, M. I. Stockman, D. J. Bergman, *Phys. Rev. Lett.* **2003**, *91*, 227402.
- [32] B. Lai, F. Cerrina, *Proc. SPIE* **1985**, *563*, 174.
- [33] R. Kingslake, R. B. Johnson, *Lens Design Fundamentals*, 2nd Ed., Elsevier Inc., Oxford, UK **2010**, Ch. 15.
- [34] M. Born, E. Wolf, *Principles of Optics*, 7th Ed., Univ. Press, Cambridge, UK **2005**, Ch. 6.6 and 8.6.
- [35] W. Singer, M. Totzeck, H. Gross, *Handbook of Optical Systems: Physical Image Formation*, Vol. 2, Wiley-VCH Verlag GmbH & Co. KGaA, Weinheim, Germany **2005**, Ch. 21.
- [36] P. B. Johnson, W. Christy, *Phys. Rev. B* **1972**, *6*, 4370.
- [37] P. Kumar, M. K. Wiedmann, C. H. Winter, I. Avrutsky, *Appl. Opt.* **2009**, *48*, 5407.

ADVANCED OPTICAL MATERIALS

Supporting Information

for *Advanced Materials.*, DOI: 10.1002/adom.201400080

Symmetry-Broken Metamaterial Absorbers as Reflectionless
Directional Couplers for Surface Plasmon Polaritons in the
Visible Range

Fan Ye, Michael J. Burns, and Michael J. Naughton**

Supporting Information

Symmetry-broken metamaterial absorbers as reflectionless directional couplers for surface plasmon polaritons in the visible range

*Fan Ye**, *Michael J. Burns*, and *Michael J. Naughton**

Table of Contents:

- I Field profiles for single-element MIM structure under resonances
- II Reflectance of Ag-Al₂O₃-Ag samples when tuning incident polarization
- III Determination of the optimum separation D for directional SPP coupling
- IV Optical measurement of the 3-set structure under illuminations with various wavelengths
- V Decay length of the directional SPP
- VI Sensitivity to the bluntness of corners of metal structures

I. Field profiles for single-element MIM structure under resonances

Figure S1 shows the field profiles for mode analysis of a single-element (symmetric) Ag-Al₂O₃-Ag structure, as discussed in Figure 2 in the main text. Figure S1a shows the simulated reflectance of this single-element MIM structure under normal incidence (angle $\alpha = 0$ in Figure 2) while tuning the length of the top metal bar (L_x), with all other parameters as defined in Figure 2 held fixed. Two modes are evident in Figure S1a, with mode 1 near 486 nm insensitive to L_x , and mode 2 near 690 nm redshifting with increasing L_x . Figure S1b shows the reflectance of the $L_x = 68$ nm structure while varying the incidence angle α . With α increasing from zero, mode 3 emerges at around 550 nm and redshifts. Profiles for H_y , E_x , E_z & S_x are shown in Figure S1c-S1j for mode 1 and mode 2 under normal incidence for $L_x = 68$ nm and all other parameters as defined in Figure 2. To illustrate mode 3, profiles of H_y , E_x , E_z & S_x are shown for $\alpha = 10^\circ$ in Figure S1k-S1n.

Electric and magnetic fields are more spatially dispersed for mode 1 than for mode 2, as shown in Figure S1c-S1f. The fact that the H_y and E_z fields distribute over a whole unit cell indicates that this mode is established by interactions between two neighbouring MIM elements. Thus, the resonance position of this mode is determined by the periodicity/pitch P_x of the structure. Tuning L_x does not affect this mode. Tuning the incident angle will affect the mode by changing the effective P_x in the light-propagating direction.

On the other hand, mode 2 is very sensitive to L_x . When L_x is tuned from 62 nm to 76 nm, the resonance position of this mode moves from 664 nm to 730 nm. From the field profiles in Figure S1g-S1j, we see the locality of this mode. Electric and magnetic fields are squeezed into the gap region between the top and bottom metal layers. The H_y field shown in Figure S1g is created by counter propagating electric currents in the two metal layers, forming an effective magnetic dipole [1]. Since L_x determines the effective dipole moment of the MIM structure, this dipole-type mode depends strongly on it. Another noticeable feature is the reflection symmetry of all simulated field profiles shown for mode 1 and mode 2, where normal incidence is applied.

Mode 3 only emerges for tilted incidence ($\alpha > 0$), where the in-plane k_x vector of incident light is matched to that of a propagating SPP by the reciprocal momentum obtained from the periodicity, $k_{\parallel} = 2\pi/P_x$, in the following way: $k_{\text{SPP}} = k_x + M k_{\parallel}$, with $M = 0, \pm 1, \pm 2, \dots$. For our adopted geometry, $M = -1$, *i.e.*, $|k_{\text{SPP}}| = |k_{\parallel} - k_x|$ (note that k_x is smaller than k_{\parallel}). So, for increasing α , k_x increases, leading to a decreased k_{SPP} , and thus increased λ_{SPP} . This is the reason for the redshifting of the mode 3 reflection minima when increasing α . The reflection symmetry for the field profiles of this mode is broken by the tilted incidence.

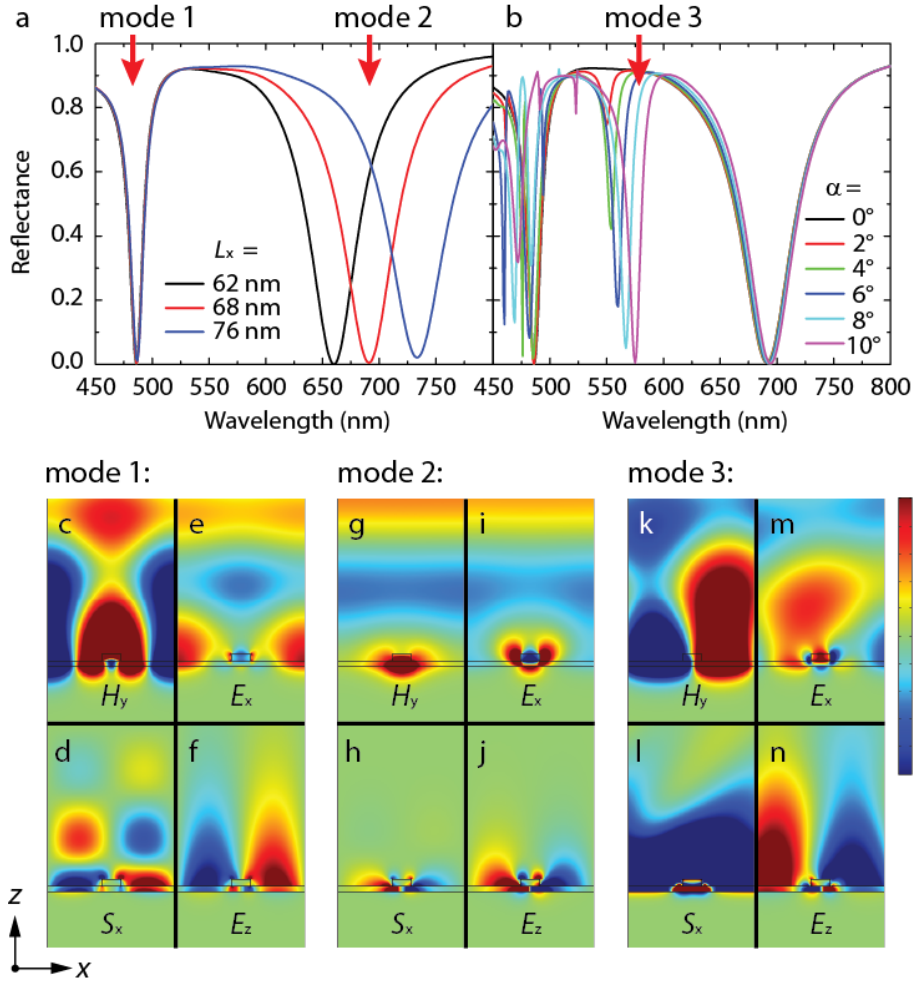


Figure S1. Field profiles for a single-element Ag-Al₂O₃-Ag structure at resonance. a) Simulated reflectance spectra under normal incidence while tuning L_x and keeping other parameters (as defined in Figure 2) fixed. b) Simulated reflectance spectra with $L_x = 68$ nm, while tuning incidence angle α . c-f) Simulated H_y (c), S_x (d), E_x (e) and E_z (f) profiles for mode 1 under $\lambda = 486$ nm normal incidence. g-j) Simulated H_y (g), S_x (h), E_x (i) and E_z (j) profiles for mode 2 under $\lambda = 690$ nm normal incidence. k-n) Simulated H_y (k), S_x (l), E_x (m) and E_z (n) profiles for mode 3 under $\lambda = 575$ nm incidence, with incidence angle $\alpha = 10^\circ$. (c)-(n) has the same geometry, with $L_x = 68$ nm and other parameters defined in Figure 2, and the same TM polarized input (H field along the y direction). Color bars: (c), (g) & (k), $(-2 \text{ to } 2) \times 10^2 \text{ Am}^{-1}$; (e), (f), (i), (j), (m) & (n), $(-1 \text{ to } 1) \times 10^5 \text{ Vm}^{-1}$; (d), (h) & (l), $(-1 \text{ to } 1) \times 10^7 \text{ Wm}^{-1}$.

II. Reflectance of Ag-Al₂O₃-Ag samples when tuning incident light polarization

Reflectance of the single-element Ag-Al₂O₃-Ag array was measured with a maximum incident angle of 3.75° , while tuning the polarization angle of the incident light, as shown in Figure S2. Polarization angle θ is defined in Figure S2a, with $\theta = 0^\circ$ representing the case when electric

field is perpendicular to the y axis. Figure S2b shows the absolute reflectance when tuning θ for a single-element Ag-Al₂O₃-Ag array with $L_x = 68$ nm, and other parameters given in Figure 2. We see that all three dips of the reflectance spectra are disappearing when increasing θ from 0° to 30° . This indicates that the y -directional periodicity does not contribute to the reflectance spectra in the visible range for x -polarized incidence, and that the x - and y -directional modes are decoupled.

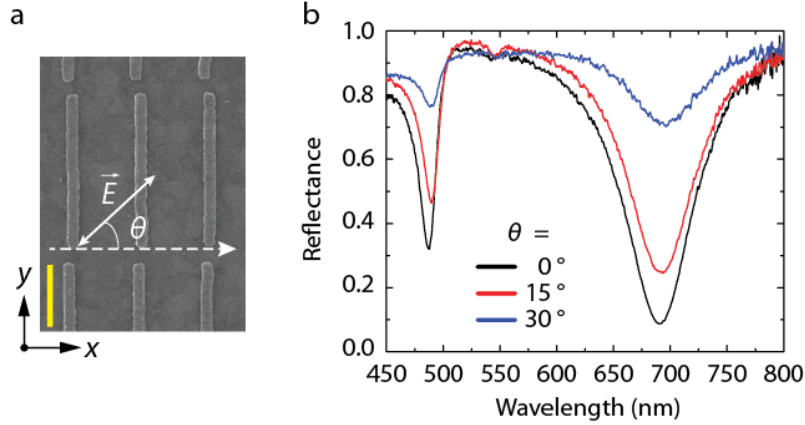


Figure S2. Reflectance measurement of a single-element Ag-Al₂O₃-Ag structure when tuning incident polarization. a) Top view SEM micrograph of an array of Ag-Al₂O₃-Ag structures, with electric field direction and polarization angle θ defined. b) Reflectance measurement of the Ag-Al₂O₃-Ag structure with $L_x = 68$ nm, under 0, 15 and 30 degree polarization incidences. Scale bar in (a), 400 nm.

III. Determination of the optimum separation D for directional SPP coupling

Figure S3 shows the reflectance and power flow along x direction for fixed pitch $P_x = 571$ nm and tuned separation D . There are two regions for the directional coupling of SPPs: one is the strong coupling region, the other is the weak coupling region. In Figure S3a, the strong coupling region corresponds to reflectance dips on the right hand side (where D/P_x close to 0.45), the weak coupling region corresponds to reflectance dips on the left hand side (where D/P_x close to 0.25). In the strong coupling region, the propagating SPP mode and the localized SPP mode strongly interact with each other, leading to the asymmetric reflectance line shape, while for the weak coupling cases the reflectance line shape is symmetric. As shown in Figure S3b, there are two local maxima for the x -component power flow (obtained by integrating time averaged power flow density over the boundary of the boundary of a unit cell). One locates in the strong coupling region (maximizing at $D/P_x = 0.46$), the other in the weak coupling region ($D/P_x = 0.24$). In the strong coupling region, the directionality mechanism is that photons are first coupled into the localized modes by element L_1 (the smaller element), then coupled to the directional SPP modes that propagate to the right, as described in the manuscript. In the weak coupling region, the directionality mechanism is based on the $\pi/2$ phase difference between the excitation and local magnetic dipole. We also notice that the power flow is larger in the strong coupling than in the weak coupling region. The reason is that in the strong coupling region, the localized SPP mode

assists to couple and transfer energy into the propagating SPP mode. Thus, more incident photons end up coupling into the propagating SPP mode. In this work, we have designed our directional coupler in the strong coupling region.

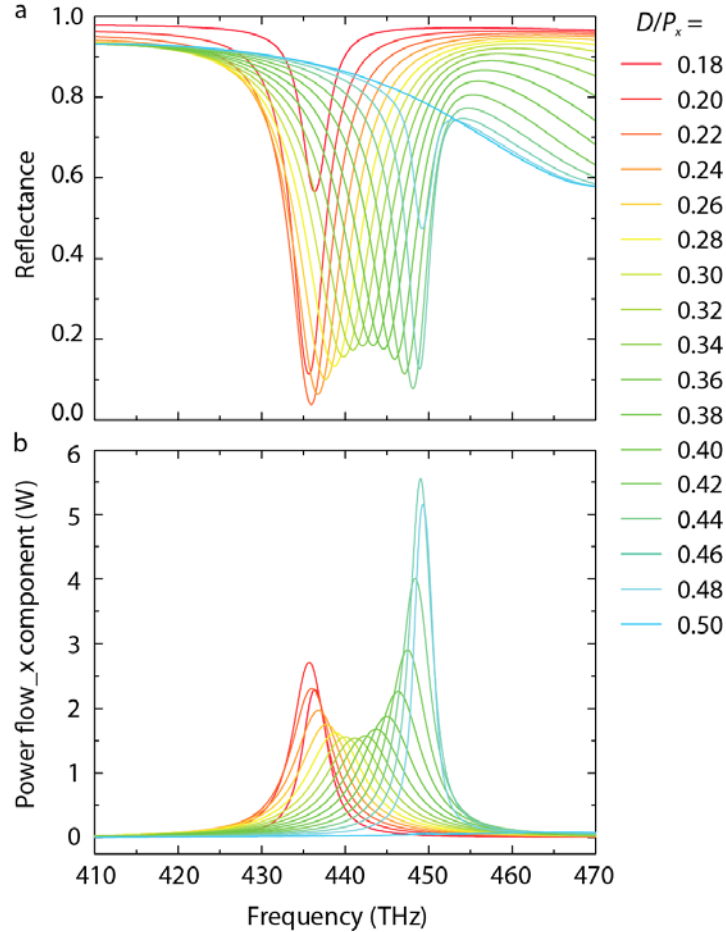


Figure S3. Reflectance (a) and power flow along x direction (b) for fixed pitch $P_x = 571$ nm and tuned separation D . Note that for $D/P_x = 0.50$, the power flow is a flat line at 0 W (blue line).

IV. Optical measurement of the 3-set structure under illuminations with various wavelengths

Figure S4 shows an optical measurement of the model structure (Figure 6) under illumination at various wavelengths, all under x-polarization. The only difference between the sample in Figure S4 and Figure 6 is that, the outer set on the left hand side in Figure S4 is pointing towards the left, instead of point towards the center. The single color light spots are extracted from a continuum of white light by a tunable light source. The diameter of the light spot is restricted to ~ 15 μm by a pinhole. Figure S4a shows a bright field image of the model structure under white light illumination. Figure S4b-S4f show bright field images of the structure under restricted light spot illumination, with tuning the incident wavelength. One can see that for wavelengths other than

642 nm, the illuminated center set region is almost as bright as the other parts of the light spot. This indicates high reflection of the center set at all other wavelengths. The right and left outer sets are all dark for wavelengths 495 nm and 555 nm, meaning no evidence for generation of propagating SPPs is observed. At 612 nm, one starts to see a weak illumination of the right-hand-side set, indicating a weak generation of propagating SPPs. At the 642 nm resonance condition for this structure, the center set is dimmed, with a strong intensity seen at the right-hand-side set. This corresponds to the situation of reflectionless generation of directional SPPs. For this sample, we measured the directionality to be 99.7% to the right and 0.3% to the left. For a longer wavelength (705 nm), the directional resonance condition breaks, and we see SPPs on both sides' outer sets. In fact, if we keep increasing the incidence wavelength, we will see a situation when the SPPs are totally coupled to the left (not shown), corresponding to the intersection region of the propagating mode with the localized mode of the longer set in Figure 4d.

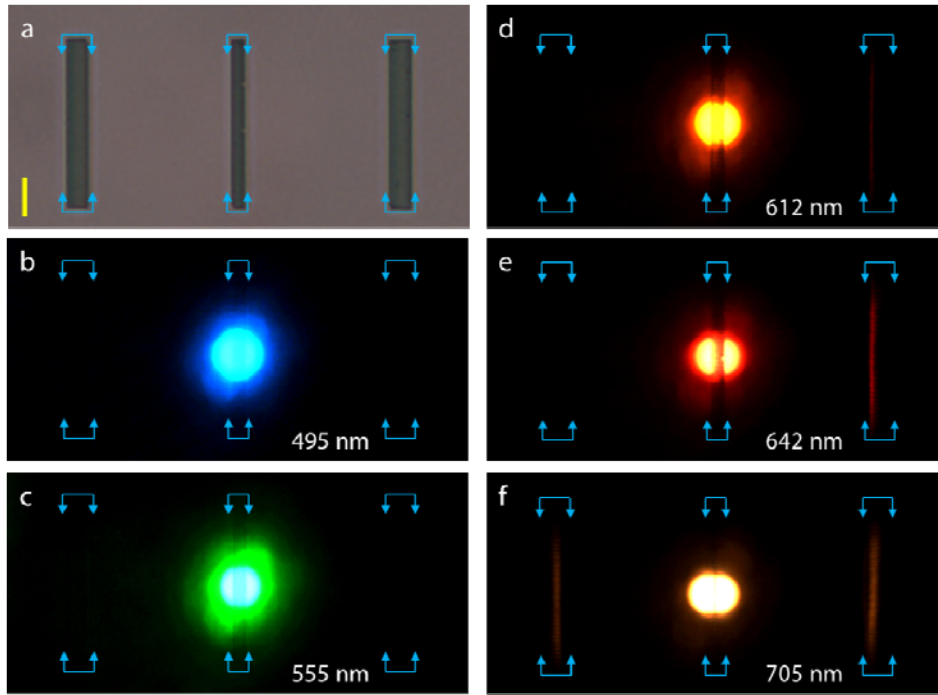


Figure S4. Three-set model sample under plane wave incidence with tuning wavelength. a) Bright field optical image of the three-set sample. b-f) Optical image of the same area as shown in (a), under illumination of a restricted light spot at wavelengths of 495 nm (b), 555 nm (c), 612 nm (d), 642 nm (e) and 705 nm (f). (a)-(e) are true color figures. (f) is a false color figure, with brightness representing intensity. Field of views are the same for all figures. Scale bar in (a), 10 μm .

V. Decay length of the directional SPP

We calculate the decay length (ℓ) at $k_{\parallel} = 10.8 \text{ rad/mm}$ ($P_x = 582 \text{ nm}$) and $D = 0.45P_x$. Figure S5a shows the simulated reflectance of the structure, with the fitted reflectance of the localized mode

(R_2) shown by red line. Figure S5b shows the corresponding integrated S_x at various positions indicated by dashed lines with the same color in Figure S5c. The reflectance minimum and the power flow density maximum coincide at 443 THz. At this frequency, the reflectance is $R_t = 2.78\%$, the fitted reflectance is $R_2 = 84.9\%$, using $R_B = 1$ for the simulations, we obtain the coupling efficiency as: $\eta = 84.5\%$. Plugging in the integrated S_x at this frequency: $I_1 = 6.14$ W, we get: $\ell = P_x I_1 / (\eta I_0) = 4.4$ μm . Figure S5b shows that for the propagating mode (443 THz) the position to choose the integrate S_x is irrelevant, consistent with the fact that at this frequency, S_x is dominated by the +x propagating SPPs.

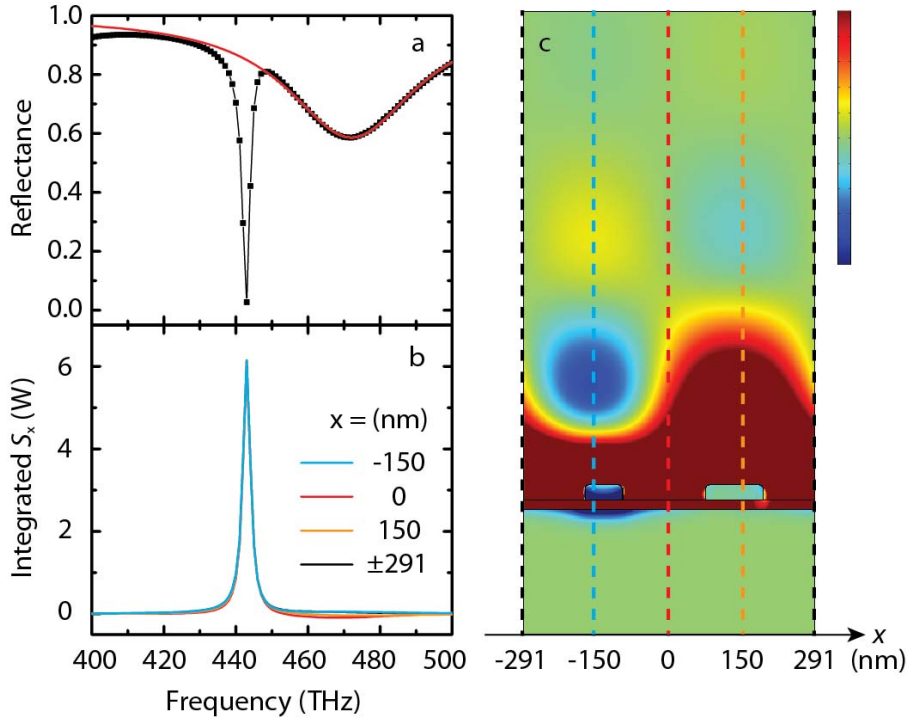


Figure S5. Calculation of decay length of the directional SPP. a) Simulated reflectance spectrum for the two-element MIM structure with $k_{||} = 10.8$ rad/ μm and $D = 0.45P_x$, and all other geometries the same as Figure 3b. Red line shows the fitted reflectance (R_2) for the localized mode centered at 472 THz. b) Integrated S_x at various positions as indicated by dashed lines with the same color in (c). c) Profile of S_x at 443 THz. Color bar in (c), from blue to red: $(-1$ to $1) \times 10^7$ Wm^{-1} .

VI. Sensitivity to the sharpness of corners of metal structures

Figure S6 shows the simulated reflectance spectra for a two element asymmetric Ag-MgF₂-Ag structure when tuning the sharpness of the top metal corners. We see that reflectance spectra do not have obvious shifts when the corners are rounded. Most modes are mainly resonating in the dielectric gap between the two metal layers, and are thus insensitive to the slight geometry

change of the top metal corners. This fact assures a more stable result against imperfections during the nanofabrication process.

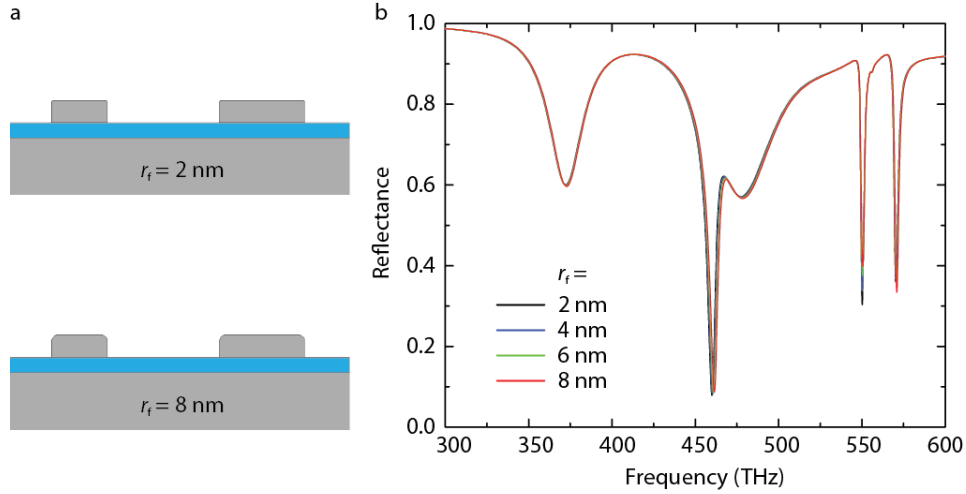


Figure S6. Simulated reflectance spectra for a two-element asymmetric Ag-MgF₂-Ag structure when tuning the sharpness of metal corners. a) Schematic cartoons showing the tuning of the filleting radius (r_f) of the top corners of the top metal layer, from 2 nm to 8 nm. b) Simulated reflectance spectra under normal incidence for a two-element asymmetric Ag-MgF₂-Ag structure with $k_{\parallel} = 11.5$ rad/ μ m, and other parameters defined in Figure 4d, while tuning (*i.e.* decreasing) the sharpness of the top corners of the top metal layer. The good overlap of all curves indicates that the sharpness/bluntness of the corners plays little role in both the propagating and localized modes in this structure.

Reference

- [1] Y. Liu, S. Palomba, Y. Park, T. Zentgraf, X. Yin, X. Zhang, *Nano Lett.* **2012**, *12*, 4853.